Appl. Phys. A (2016) 122:812
DOI 10.1007/s00339-016-0306-2

Applied Physics A
Materials Science & Processing

The phase structure and electrochemical performance of $xLi_2MnO_3 \cdot (1-x)LiNi_{1/3}Co_{1/3}Mn_{1/3}O_2$ during the synthesis and charge–discharge process

Ting Yuan[1] · HongQuan Liu[1] · YiJie Gu[1] · HongZhi Cui[1] · YanMin Wang[1]

Received: 7 June 2016 / Accepted: 22 July 2016 / Published online: 11 August 2016

Abstract The lithium-rich layered $xLi_2MnO_3 \cdot (1-x)LiNi_{1/3}Co_{1/3}Mn_{1/3}O_2$ materials were simply prepared by the molten-salt method. The effects of reaction temperature and x value on the phase structure and electrochemistry were systemically studied by X-ray diffraction, galvanostatical charge/discharge and electrochemical impedance spectroscopy (EIS). It has been found that the obtained phase is sensitive to the reaction temperature and composition. A layered rock-salt form with hexagonal α-$NaFeO_2$-type structure occurs at 700 °C, while a spinel $LiMn_2O_4$ becomes the main phase at 800 °C. Besides, a spinel $Li_4Mn_5O_{12}$ component can be found in the lithium-rich layered material when x value decreases to 0.4. The $0.4Li_2MnO_3 \cdot 0.6LiNi_{1/3}Co_{1/3}Mn_{1/3}O_2$ material can deliver a high initial discharge capacity of 218 $mAhg^{-1}$ under 20 mAg^{-1} current rate, then increase to the maximum 241 $mAhg^{-1}$ after 4 cycles. It is confirmed by different cycle dQ/dV profile change that the layer rock-salt transforms into the two phases with the layer rock-salt phase and the spinel phase step by step. According to the EIS analysis, the $0.4Li_2MnO_3 \cdot 0.6LiNi_{1/3}Co_{1/3}Mn_{1/3}O_2$ sample with the better electrochemical performance shows the smaller charge transfer resistance and Warburg impedance associated with Li-ion diffusion through cathode, which is attributed to contribution from a fast 3D Li-ion diffusion channel of appropriate $Li_4Mn_5O_{12}$ phase.

1 Introduction

Lithium-rich cathode materials have been the research focus of electrode materials due to their high discharge specific capacity when cycled above 4.5 V, which represents an important milestone in the material design for advanced lithium-ion batteries [1–3]. However, there are the following technical bottlenecks for their industry application: (1) the large irreversible capacity loss after first cycle; (2) the insufficient cycling performance at the high voltages; (3) the poor rate capability; (4) the voltage attenuation caused by the phase transformation during cycling process. The huge irreversible capacity loss has been attributed to the elimination of oxygen atom and lithium-ion vacancies from the layered lattice at the end of the first charge, which is also source of higher special capacity than other materials [4]. The poor rate capability could be related to the low electronic conductivity associated with the surface phase or the thick SEI layer, which is formed by a reaction of the cathode surface with the electrolyte. In addition, transport behavior in the bulk phase is also a key factor for the rate capacity, cycle life and voltage fade. Many researchers devote themselves to deeply analyzing reasons for voltage fade, structural transformation and roles of transition metals [5–7]. In order to overcome the above problems, in recent years much effort has been devoted to the preparation of the

Electronic supplementary material The online version of this article (doi:10.1007/s00339-016-0306-2) contains supplementary material, which is available to authorized users.

✉ HongQuan Liu
15192090861@163.com

YiJie Gu
guyijie@sdust.edu.cn

HongZhi Cui
cuihongzhi1965@sdust.edu.cn

[1] College of Materials Science and Engineering, Shandong University of Science and Technology, Qingdao 266590, China

composites that integrate both high-power characteristics and rate capability to meet the ever-increasing demand for new cathode materials of lithium-ion batteries [8–12]. All bottlenecks are closely relative to the fine structure of prepared phase and the structure change during charge–discharge process. All the solutions to improve electrochemical performance are based on adjustment of structure such as element composition design, conductive layer and morphology control [12–15].

The methods for preparing lithium-rich cathode materials include molten salt, co-precipitation spray pyrolysis, hydrothermal, simple solid-phase, carbon-thermal reduction and others [16]. Among them, the molten-salt method is one of the most versatile and simple methods to prepare various metal oxides with controlled morphology and tailored physical and electrochemical properties [17, 18]. Previously, one pot molten-salt synthesis method was used for the preparation of layered cathodes, namely $LiCoO_2$, $Li(Co_{1-x}Al_x)O_2$, $Li(Ni_{1/3}Co_{1/3}Mn_{1/3})O_2$, $Li(Ni_{0.5}Co_{0.5})O_2$ and $Li(Ni_{0.5}Co_{0.4}Al_{0.1})O_2$ using 0.5MNaCl:0.5MKCl salt [19].

In this work, the molten-salt method was adopted to prepare our samples. The phase structure change under different synthetic condition was discussed, and the effect of phase structure on electrochemistry was analyzed by the subtle analysis of diffraction peak and redox peak change in the dQ/dV plots at different charge/discharge times. The effect of different phase structures on Li-ion transport nature in the battery was discussed by the EIS analysis, which explains the electrochemical performance difference for samples with different phase structures.

2 Experimental

Target samples ($xLi_2MnO_3\cdot(1-x)LiNi_{1/3}Co_{1/3}Mn_{1/3}O_2$) were prepared by the molten-salt method as follows. Firstly, Li_2CO_3, $MnCO_3$, $Co(NO_3)_2\cdot 6H_2O$ and $Ni(CH_3COO)_2\cdot 4H_2O$ were mixed with stoichiometric ratio of $(3x+3):(2x+1):(1-x):(1-x)$. Then the above mixture was added to the KCl, NaCl or KCl–NaCl (with stoichiometric ratio of 1:1) salts in a crucible. Next, the crucible was held at 200 °C for 1 h and then annealed at 700–825 °C (due to melting point difference among molten salts) for another 10 h followed by cooling at the room temperature to obtain black precipitates. Finally, after the precipitates were soaked and washed by the distilled water for several times, the residue was dried at 80 °C. To clearly distinguish the products, six kinds of compounds have been named as X5-KCl, X5-NaCl, X5-700, X5-800, X4-700 and X3-700 as given in Table 1.

The phases of samples were characterized by X-ray diffraction on a Rigaku D/MAX-2000 powder diffractometer at 20 kV. The charge–discharge measurements of electrodes were done by cell testing platform LAND CT2001A. Charge–discharge tests were performed at a current rate from 20 to 100 mAg^{-1} over a potential range between 2.0 and 4.8 V at room temperature. EIS measurement was conducted with an electrochemical workstation (Zahner Zennium) using an amplitude of 5 mV and a frequency range from 100 kHz to 0.1 Hz. The EIS spectra were performed at the open-circuit voltage about 2.76 V with deviation less than 0.1 V after 4 times cycle. The cathodes for testing cells were fabricated by mixing 80:12:8 (w/w/w) ratio of active material about 0.4 g, a carbon electronic conductor (acetylene black) and polytetrafluoroethylene (PTFE), respectively, using NMP as the solvent and then compressed onto the aluminum. The electrode was made after being dried over 12 h at 120 °C in a vacuum oven. The electrode area in a cell is 0.95 cm^2. The cells were assembled in glove box. In the test cells, lithium metal and porous polypropylene film served as counter electrode and separator, respectively. The electrolyte solution was 1.0 M $LiPF_6$ in ethylene carbonate and diethyl carbonate with a weight ratio of 1:1.

3 Results and discussion

Figure 1 shows XRD patterns of the X5-KCl, X5-NaCl, X5-700 and X5-800 samples in the range of scattering angles from 10° to 80°. In Fig. 1a, the main XRD patterns of the X5-KCl, X5-NaCl and X5-700 samples can be indexed to the layered rock-salt phase with hexagonal α-$NaFeO_2$-type structure with a space group of $R\bar{3}m$. A low-intensity peak near $2\theta = 21°$–$23°$ (denoted with the solid ellipse) for each pattern arises from super-lattice ordering of Li and Mn in the transition-metal layer, which is the characteristic of Li-rich material close to the Li_2MnO_3 composition with C/2m space group. In addition to the main crystal phase, the X5-KCl, X5-NaCl samples were indexed to the spinel phase at 30.6°, 36.5°, 63.5°, while the X5-700 sample is the pure phase. It can be seen that the KCl–NaCl salt is more beneficial to the crystallization of the layer phase. In Fig. 1b, the main crystal phase of the X5-800 sample is indexed to the cubic spinel $LiMn_2O_4$ phase with a space group of Fd-3m. Zhao et al. [20] reported that the $Li_{1.2}Co_{0.4}Mn_{0.4}O_2$ powder annealed at 850 °C is pure Li-rich phase using an improved molten-salt method. The different results are attributed to the [20] conditions. The Li-rich phase is unstable above 800 °C under our synthesis condition, which easily transforms to the spinel structure.

The SEM images of the X5-700, X5-800 samples are shown in Fig. 2. The aggregated particles of the X5-700 sample are shown in Fig. 2a, and the smaller primary

Table 1 Identification of samples under the different processes

Serial number	Stoichiometric ratio $xLi_2MnO_3 \cdot (1-x)LiNi_{1/3}Co_{1/3}Mn_{1/3}O_2$	Reaction temperature (°C)	Reaction time (h)	Molten salt
X5-KCl	$0.5Li_2MnO_3 \cdot 0.5LiNi_{1/3}Co_{1/3}Mn_{1/3}O_2$	800	10 h	KCl
X5-NaCl	$0.5Li_2MnO_3 \cdot 0.5LiNi_{1/3}Co_{1/3}Mn_{1/3}O_2$	825	10 h	NaCl
X5-700	$0.5Li_2MnO_3 \cdot 0.5LiNi_{1/3}Co_{1/3}Mn_{1/3}O_2$	700	10 h	KCl–NaCl
X4-700	$0.4Li_2MnO_3 \cdot 0.6LiNi_{1/3}Co_{1/3}Mn_{1/3}O_2$	700	10 h	KCl–NaCl
X3-700	$0.3Li_2MnO_3 \cdot 0.7LiNi_{1/3}Co_{1/3}Mn_{1/3}O_2$	700	10 h	KCl–NaCl
X5-800	$0.5Li_2MnO_3 \cdot 0.5LiNi_{1/3}Co_{1/3}Mn_{1/3}O_2$	800	10 h	KCl–NaCl

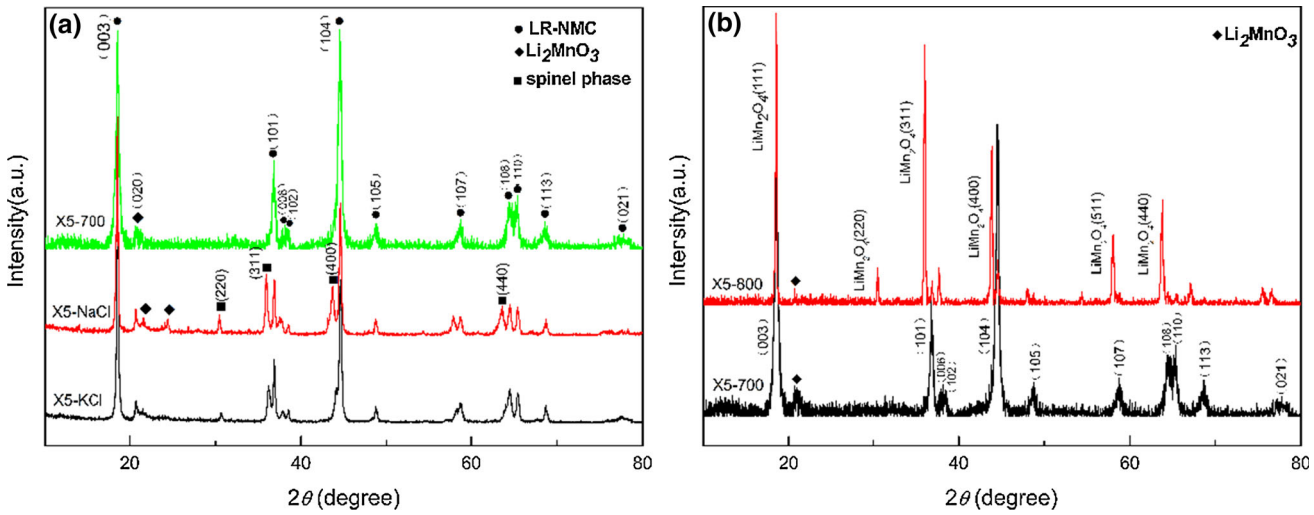

Fig. 1 The XRD patterns of the X5-KCl, X5-NaCl, X5-700 and X5-800 samples

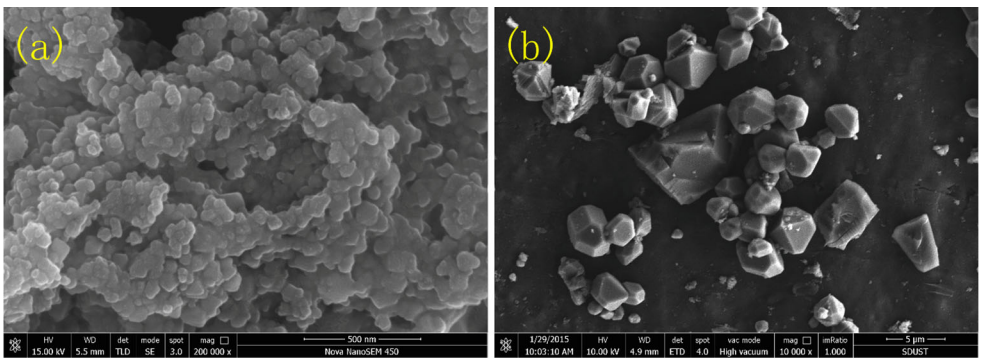

Fig. 2 The SEM images of the X5-700 (**a**), X5-800 (**b**) samples

particles are generally in the range of 100–200 nm in diameter. The morphology is coincident with other literature [21]. In Fig. 2b, the morphology of the X5-800 sample presents a wide particle distribution with an polyhedral shape, which is the typical morphology of spinel $LiMn_2O_4$ structure [22].

The discharge special capacities of the X5-700 sample under different current rates are shown in Fig. 3. The X5-700 sample only delivers the initial discharge capacity of 150 $mAhg^{-1}$, but displays higher discharge capacity of 200 $mAhg^{-1}$ after 8 cycles at current rate of 20 mAg^{-1}. The obvious discharge capacity increase shown in Fig. 3 is attributed to stepwise activation of Li_2MnO_3 [23]. As current density of discharge increases, discharge capacity decreases from 200 to 110 $mAhg^{-1}$. Severely cracked particles may finally become fragmented pieces and no longer be available for reversible Li-ion insertion/extraction, resulting in capacity degradation.

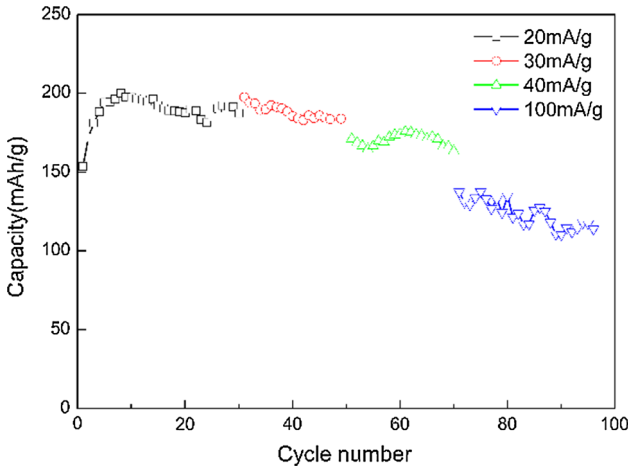

Fig. 3 Rate performances of the X5-700 sample under different current rates

On the basis of the above experimental results, the effect of mole ratio between Li_2MnO_3 and $LiNi_{1/3}Co_{1/3}Mn_{1/3}O_2$ on phase stability and electrochemical properties was further investigated. Figure 4a shows the XRD patterns in the range of scattering angles from 10° to 80° for the X5-700, X4-700 and X3-700 samples. The XRD patterns of main phase are indexed to hexagonal α-$NaFeO_2$-type structure. The additional XRD pattern at about 31° occurs for X4-700 and X3-700 samples, which are indexed to the (220) peak of spinel phase $Li_4Mn_5O_{12}$ (PDF#46-0810). In order to further confirm the $Li_4Mn_5O_{12}$ with the spinel structure, XRD data shown in Fig. 4 were analyzed in detail. Firstly, as shown in Fig. 4b, there is the shoulder peak or split peak denoted by a pentagram for the X4-700 or X3-700 sample, respectively, which may be the evidence of the (311) peak for a spinel $Li_4Mn_5O_{12}$ phase. Secondly, as the Li_2MnO_3 content decreases, $Li_4Mn_5O_{12}$ phase obviously increases, which accounts for $Li_4Mn_5O_{12}$ phase in Li_2MnO_3–$LiMO_2$ structure easily occurring. This phenomenon was different from other reported literatures, which coexists with Li-rich layer structure by integration with the spinel $LiMn_2O_4$ phase [24]. Finally, the evidence of a $Li_4Mn_5O_{12}$ phase is also shown in Fig. 4c. The intensity of (110) and (108) peak is comparative in hexagonal α-$NaFeO_2$-type structure, while the experimental results show that relative intensity of the (108) peak increases as Li_2MnO_3 content decreases. The enhanced intensity of (108) peak is attributed to contribution from (440) peak of $Li_4Mn_5O_{12}$ (PDF#46-0810). According to the above analysis, Li_2MnO_3 component of Li-rich material makes layer structure stable, when x value exceeds 0.5. A $Li_4Mn_5O_{12}$ phase easily occurs when x is less than or equal to 0.4. The SEM images of the X3-700, X4-700 and X5-700 samples are shown in SFigure 1 of supplementary information. There is no obvious morphology difference among the three samples.

To investigate the effect of the ratio between Li_2MnO_3 and $LiMO_2$ phase on the electrochemical performances of the as-synthesized samples, the charge–discharge cycling was conducted at room temperature between 2.0 and 4.8 V at 20 mAg^{-1}, and the results are displayed in Fig. 5. Two charging regions corresponding to different electrochemical reactions can be clearly observed in the first charge curve of the three samples. The first region, characterized by a sloping voltage profile, is attributed to the removal of lithium from the $LiNi_{1/3}Co_{1/3}Mn_{1/3}O_2$ component with a concomitant oxidation of Ni^{2+} to Ni^{4+} [25]. During the sloping charging course, inactivated Li_2MnO_3 in the composite structure can act as a reservoir of surplus lithium, which can diffuse from the transitional metal layers into the adjacent lithium-depleted layers in order to stabilize the crystal structure at low lithium loadings. The

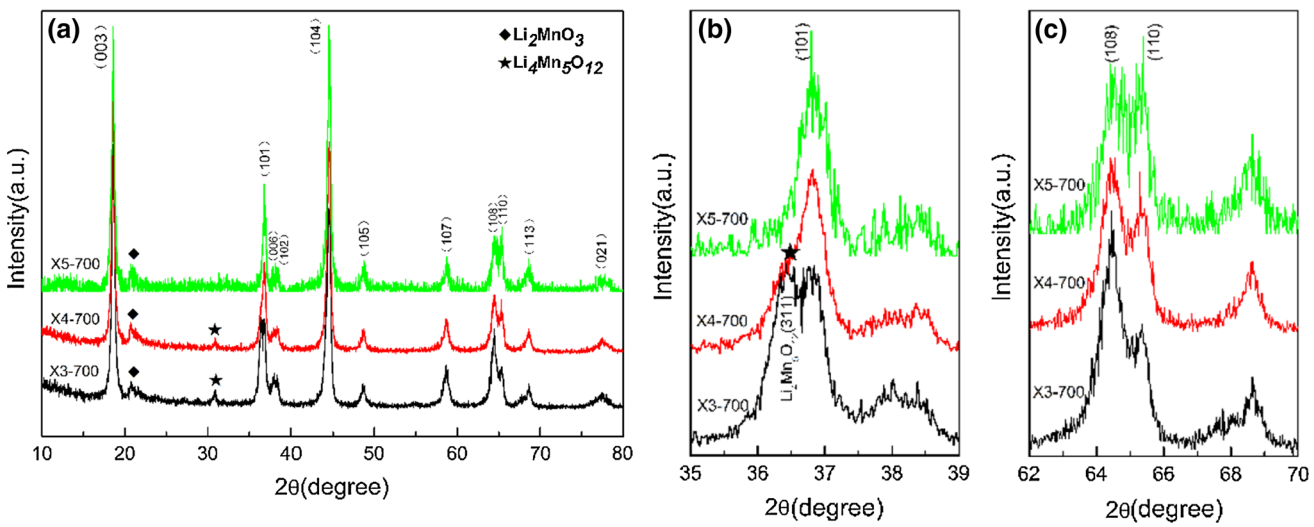

Fig. 4 The XRD patterns of the X5-700, X4-700 and X3-700 samples. **a** Full spectrum, **b, c** location larger spectrum

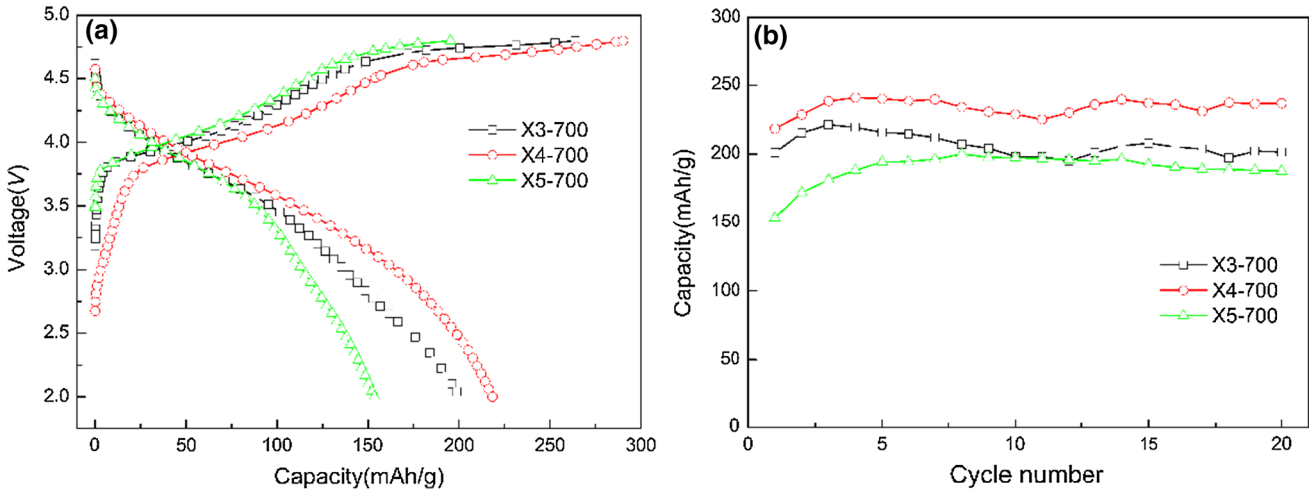

Fig. 5 Initial charge and discharge profile (**a**) cycle performance (**b**) for the X5-700, X4-700, X3-700 samples under 20 mAg^{-1} during 2.0–4.8 V

second region, characterized by a long plateau around 4.65 V, can be attributed to the electrochemical activation process that extracts a net loss of Li_2O from the Li_2MnO_3 component [4]. The initial discharge capacities of the X5-700, X4-700 and X3-700 samples reach 152, 218 and 200 $mAhg^{-1}$, respectively. It is the reason of obvious special capacity difference among samples that the Li_2MnO_3 component in the X5-700 sample is not adequately activated. The explanation can be confirmed from the cycle performance data in Fig. 5b, special capacity of the X5-700 sample reaches the maximum value after 8 times cycle, while those of X3-700 and X4-700 samples reach the maximum value 218, 241 $mAhg^{-1}$ after 3 or 4 times cycle, respectively. This also confirms that the existence of $Li_4Mn_5O_{12}$ enhances the activation ability of the Li_2MnO_3 phase. From the cycle performance shown in Fig. 5b, a fluctuation of special capacity occurs for the X4-700 and X3-700 samples, while the phenomenon does not occur for the X5-700 samples. Essential reason needs to be further researched.

To further evaluate the charge–discharge process of the X4-700 sample, the discharge curves of the 1st, 4th, 7th, 14th, 18th, 20th are presented in Fig. 6. The discharge special capacity reaches the maximum value at 4th discharge profile and then decreases slowly. It is well known that the voltage degradation during the cycling process seriously hinders their applications, because voltage fade would result in a dramatic decrease in energy density. The voltage degrade of the X4-700 sample is not obvious, which is similar to other literature [26].

Examining the charge branch of the dQ/dV plots shown in Fig. 7a, two major peaks are clearly observed at first charge: The relative sharp peak at 4.7 V (denoted as P1) is associated with the removal of lithium ions along with the

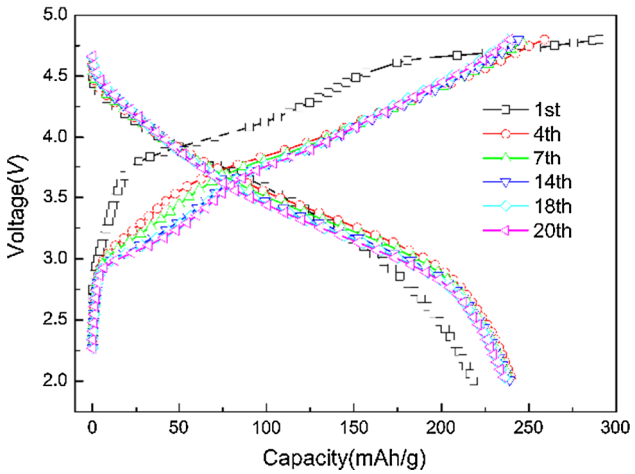

Fig. 6 Charge and discharge profile for the X4-700 sample under 20 mAg^{-1} during 2.0–4.8 V

simultaneous oxygen evolution. Another broad one at about 4.0 V (denoted as P2) is ascribed to oxidation of Ni^{2+} and Co^{3+} ions [27, 28]. At 4th charge process, the P1 peak disappears, and the P2 peak shifts to low voltage, which is the new oxide containing Ni and Co ion with other value states. A platform occurs from 3.1 to 3.4 V at 4th charge process, which evolves to P3 peak at 20th charge process. The P3 peak can be attributed to the formation of the spinel phase, which confirms the phase change during charge–discharge process [29].

The discharge branch of the dQ/dV plots is shown in Fig. 7b. At first discharge, there is a main peak (R2) at about 3.75 V, and three shoulder peaks occur at about 3.25 V (R4), 3.5 V (R3) and 4.3 V (R1), respectively. The reduce peak at 3.75 V can be attributed to the reduce reaction of $Ni^{2+/3+/4+}$ or $Co^{3+/4+}$ [30]. The shoulder peak

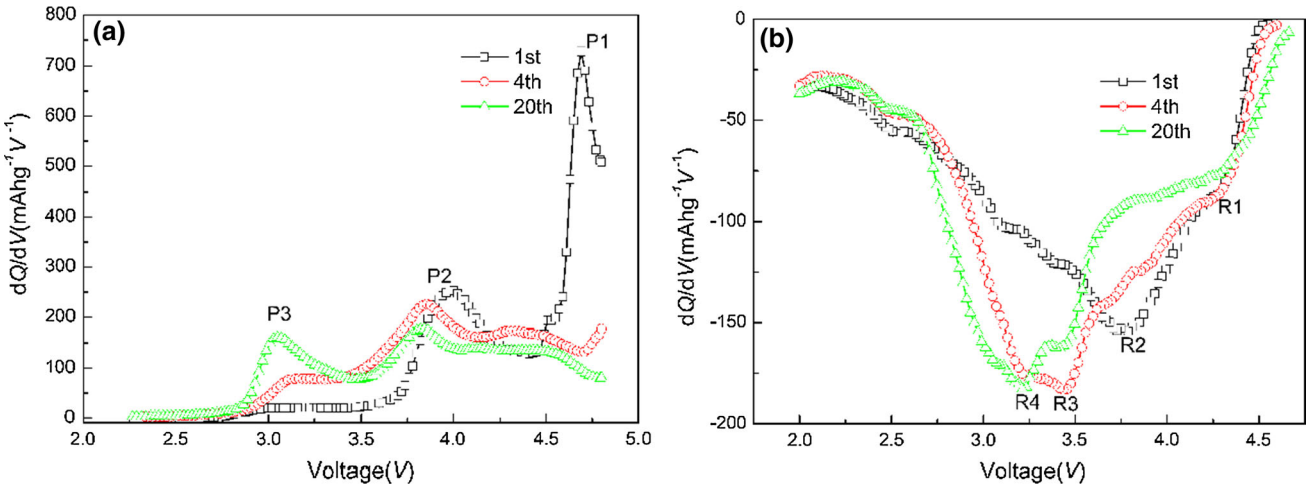

Fig. 7 dQ/dV profile for the X4-700 sample **a** charge course **b** discharge course

(R4) at 3.25 V is associated with value state change of $Mn^{3+/4+}$ in the spinel phase. The shoulder peaks at about 3.5 and 4.3 V are corresponding to $Mn^{3+/4+}$ in the layer structure and the spinel phase, respectively [5]. During the 4th discharge process, the main peak at 3.75 V transfers to a shoulder peak, and the peak at about 3.5 V turns into the main peak. The shoulder peak at 3.75 V becomes weaker during the 20th discharge process, and the peaks at about 3.5 V change into a shoulder peak. Another peak at about 3.25 V becomes the strongest as discharge process goes, which accounts for the increasing formation of spinel phase with the electrode structure [31]. The peak (R4) at 3.25 V, corresponding to the occupation of Li within octahedral sites associated with the reduction of Mn^{4+}, demonstrates an increasing contribution to the total discharge capacity with a gradual shift to lower potentials during the cycling process [32].

As shown in SFigure 2 of supplementary information, rate capability of the X4-700 sample is performed from current densities of 20–100 mAg^{-1}. Special capacity doesn't obviously fade at 30 mAg^{-1} and reach about 225 $mAhg^{-1}$. While the charge–discharge current is over 40 mAg^{-1}, special capacity obviously decreases and is about 100 $mAhg^{-1}$ at 100 mAg^{-1}. The difference in resistance among $xLi_2MnO_3{\cdot}(1-x)LiNi_{1/3}Co_{1/3}Mn_{1/3}O_2$ samples is revealed by electrochemical impedance spectroscopy in Fig. 8. The equivalent circuit is shown in inset of Fig. 8 by fitting the EIS data, which is similar to other literatures [33, 34]. A linear feature is observed at low frequency, which resembles a Warburg type response, attributable to the solid-state diffusion of Li ion into active mass. On the basis of low-frequency part in Fig. 8, the Warburg factor (σ) can be obtained by the formula $Z' = R_e + R_{ct} + \sigma\omega^{-1/2}$ [35]. So the σ for the X3-700, X4-700 and X5-700 samples is 237.4, 110.8 and 475.5 $\Omega Hz^{1/2}$,

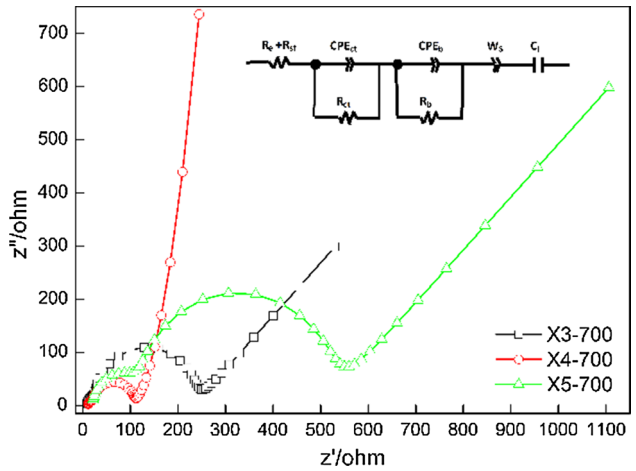

Fig. 8 AC impedance spectra and equivalent circuit for the X3-700, X4-700, X5-700 samples

respectively. According to the formula $D_{Li^+} = 0.5R^2T^2/n^4A^2F^4C^2\sigma^2$, the values of the resistance and diffusion coefficient for each sample are shown in Table 2 [36]. The X3-700 and X4-700 samples show the smaller R_b due to the occurrence of the $Li_4Mn_5O_{12}$ phase and the more layer component. There is the biggest value of the diffusion coefficient for the X4-700 sample because $Li_4Mn_5O_{12}$ can effectively reduce the barrier for Li-ion diffusion. Generally speaking, the bigger diffusion

Table 2 Resistance and lithium-ion diffusion coefficients of each sample

Sample	R_{e+sf} (Ω)	R_{ct} (Ω)	R_b (Ω)	D_{Li}^+ ($cm^2\ s^{-1}$)
X3-700	8.308	209.1	14.38	2.460836×10^{-15}
X4-700	10.81	9.527	85.06	5.527517×10^{-15}
X5-700	20.48	92.12	395.4	1.339122×10^{-15}

coefficient is, the bigger discharge capacity is. So the results are consistent with the above charge–discharge curve results.

4 Conclusion

A series of $xLi_2MnO_3\cdot(1-x)LiNi_{1/3}Co_{1/3}Mn_{1/3}O_2$ materials are simply synthesized by the molten-salt method. It has been found that the obtained phase is sensitive to the temperature and composition, and high temperature exceeding 800 °C induces the formation of the $LiMn_2O_4$ phase. A spinel $Li_4Mn_5O_{12}$ component can be found in the $xLi_2MnO_3\cdot(1-x)LiNi_{1/3}Co_{1/3}Mn_{1/3}O_2$ material, when x value is less than or equal to 0.4. The $0.4Li_2MnO_3$-$0.6LiNi_{1/3}Co_{1/3}Mn_{1/3}O_2$ material can deliver a high initial discharge capacity of 218 $mAhg^{-1}$ under 20 mAg^{-1} current rate, then increase to 241 $mAhg^{-1}$ after 4 cycles, which confirms that the existence of $Li_4Mn_5O_{12}$ enhances the activation ability of the Li_2MnO_3 phase. According to the dQ/dV profile, there is the phase change from layer structure to spinel phase during the charge–discharge process. From the EIS analysis, the $0.4Li_2MnO_3\cdot0.6LiNi_{1/3}Co_{1/3}Mn_{1/3}O_2$ sample shows the better electrochemical performance due to the smaller charge transfer resistance and Warburg impedance, which is attributed to the contribution from a fast 3D Li-ion diffusion channel of appropriate $Li_4Mn_5O_{12}$ phase.

Acknowledgments The authors would like to thank the financial supports from the TaiShan Scholars Project of Shandong (TS20110828), Shandong Natural Science Foundation Project (Grant No. ZR2015EM013) and a Project of Shandong Province Higher Educational Science and Technology Program (Grant No. YA07).

References

1. J. Lee, A. Urban, X. Li, D. Su, G. Hautier, G. Ceder, Science **343**, 519–522 (2014)
2. M. Sathiya, A.M. Abakumov, D. Foix, G. Rousse, K. Ramesha, M. Saubanère, M.L. Doublet, H. Vezin, C.P. Laisa, A.S. Prakash, D. Gonbeau, G.V. Tendeloo, J.M. Tarascon, Nat. Mater. **14**, 230–238 (2015)
3. M. Sathiya, G. Rousse, K. Ramesha, C.P. Laisa, H. Vezin, M.T. Sougrati, M.L. Doublet, D. Foix, D. Gonbeau, W. Walker, A.S. Prakash, M. BenHassine, L. Dupont, J.M. Tarascon, Nat. Mater. **12**, 827–835 (2013)
4. M. Gu, I. Belharouak, J. Zheng, H. Wu, J. Xiao, A. Genc, K. Amine, S. Thevuthasan, D.R. Baer, J.G. Zhang, N.D. Browning, J. Liu, C. Wang, ACS Nano **7**(1), 760–767 (2013)
5. Y. Wu, C. Ma, J.H. Yang, Z.C. Li, L.F. Allard, C.D. Liang, M.F. Chi, J. Mater. Chem. **A3**, 5385–5391 (2015)
6. C.H. Shen, S.Y. Shen, F. Fu, C.G. Shi, H.Y. Zhang, M.J. Pierre, H. Su, Q. Wang, B.B. Xu, L. Huang, J.T. Li, S.G. Sun, J. Mater. Chem. A **3**, 12220–12229 (2015)
7. T. Kawaguchi, K. Fukuda, K. Tokuda, M. Sakaida, T. Ichitsubo, M. Oishi, J. Mizuki, E. Matsubara, Phys. Chem. Chem. Phys. **17**, 14064–14070 (2015)
8. M. Jiang, B. Key, Y.S. Meng, C.P Grey, Chem. Mater. **21**(13), 2733–2745 (2009)
9. Q. Li, G.S. Li, C.C. Fu, D. Luo, J.M. Fan, D.J. Xie, L.P. Li, J. Mater. Chem. A **3**, 10592–15602 (2015)
10. P.K. Nayak, J. Grinblat, M. Levi, O. Haik, E. Levi, Y.K. Sun, N. Munichandraiah, D. Aurbach, J. Mater. Chem. A **3**, 14598–14608 (2015)
11. B. Xu, C.R. Fell, M. Chi, Y.S. Meng, Energy Environ. Sci. **4**, 2223–2233 (2011)
12. L. Chen, Y.F. Su, S. Chen, N. Li, L.Y. Bao, W.K. Li, Z. Wang, M. Wang, F. Wu, Adv. Mater. **26**, 6756–6760 (2014)
13. J. Zheng, W.H. Kan, A. Manthiram, ACS Appl. Mater. Interface **7**(12), 6926–6934 (2015)
14. X.P. Zhang, S.W. Sun, Q. Wu, N. Wan, D. Pan, Y. Bai, J. Powder Sour. **282**, 378–384 (2015)
15. F. Wu, N. Li, Y.F. Su, H.F. Shou, L.Y. Bao, W. Yang, L.J. Zhang, R. An, S. Chen, Adv. Mater. **25**, 3722–3726 (2013)
16. J.H. Yan, X.B. Liu, B.Y. Li, RSC Adv. **4**, 63268–63284 (2014)
17. M.V. Reddy, N. Sharma, S. Adams, R.P. Rao, V.K. Peterson, B.V.R. Chowdari, RSC Adv. **5**, 29535–29544 (2015)
18. M.V. Reddy, G.V.S. Rao, B.V.R. Chowdari, J. Phys. Chem. C **111**(31), 11712–11720 (2007)
19. M.V. Reddy, B.D. Tung, L. Yang, N.D.Q. Minh, K.P. Loh, B.V.R. Chowdarib, J. Power Sour. **225**, 374–381 (2013)
20. Y.J. Zhao, W.F. Ren, R. Wu, Y.Y. Yue, Y.C. Sun, J. Solid State Electron. **17**, 2259–2267 (2013)
21. Y.J. Zhao, W.F. Ren, R. Wu, Y.Y. Yue, Y.C. Sun, Chem. Eur. **J21**, 7503–7510 (2015)
22. M.Y. Mo, C.C. Ye, K. Lai, Z.Z. Huang, L.C. Zhu, G.Z. Ma, H.Y. Chen, K.S. Hui, Appl. Surf. Sci. **276**, 635–640 (2013)
23. D.L. Ye, B. Wang, Y. Chen, G. Han, Z. Zhang, H.J. Denisa, J. Zou, L.Z. Wang, J. Mater. Chem. A **2**, 18767–18774 (2014)
24. X. Feng, Z.Z. Yang, D.C. Tang, Q.Y. Kong, L. Gu, Z.X. Wang, L.Q. Chen, Phys. Chem. Chem. Phys. **17**, 1257–1264 (2015)
25. S.H. Kang, M.M. Thackeray, Electrochem. Commun. **11**(4), 748–751 (2009)
26. P.K. Nayak, J. Grinblat, M. Levi, B. Markovsky, D. Aurbach, J. Electro. Chem. Soc. **161**(10), A1534–A1547 (2014)
27. C.S. Johnson, N.C. Li, C. Lefief, J.T. Vaughey, M.M. Thackeray, Chem. Mater. **20**(19), 6095–6106 (2008)
28. D. Buchholz, J. Li, S. Passerini, G. Aquilanti, D.D. Wang, M. Giorgetti, Chem. Electron. Chem. **2**, 85–97 (2015)
29. S. Ramesh, S.A. Rajalakshmi, J.R. Dahn, Chem. Mater. **27**, 757–767 (2015)
30. J.R. Croy, D. Kim, M. Balasubramanian, J. Electrochem. Soc. **159**(6), A781–A790 (2012)
31. J. Zheng, M. Gu, J. Xiao, P. Zuo, C. Wang, J.G. Zhang, Nano Lett. **13**(8), 3824–3830 (2013)
32. B. Song, H. Liu, Z. Liu, P. Xiao, M.O. Lai, L. Lu, Sci. Rep. **3**, 3094 (2013)
33. M.V. Reddy, R.G.V. Subba, B.V.R. Chowdari, J. Phys. Chem. C **11**, 11712–11720 (2007)
34. M.V. Reddy, R.G.V. Subba, B.V.R. Chowdari, J. Mater. Chem. **21**, 10003–10011 (2011)
35. R. Cai, S.M. Jiang, X. Yu, B.T. Zhao, H.T. Wang, Z.P. Shao, J. Mater. Chem. **22**, 8013–8021 (2012)
36. J.Y. Xiang, J.P. Tu, Y.Q. Qiao, X.L. Wang, J. Zhong, D. Zhang, C.D. Gu, J. Phys. Chem. C **115**(5), 2505–2513 (2011)